

8-1-2022

## Polar Alignment of Massive Retrograde Circumbinary Discs

Charles Abod

Follow this and additional works at: <https://digitalscholarship.unlv.edu/thesesdissertations>



Part of the [Astrophysics and Astronomy Commons](#)

---

### Repository Citation

Abod, Charles, "Polar Alignment of Massive Retrograde Circumbinary Discs" (2022). *UNLV Theses, Dissertations, Professional Papers, and Capstones*. 4493.  
<http://dx.doi.org/10.34917/33690263>

This Thesis is protected by copyright and/or related rights. It has been brought to you by Digital Scholarship@UNLV with permission from the rights-holder(s). You are free to use this Thesis in any way that is permitted by the copyright and related rights legislation that applies to your use. For other uses you need to obtain permission from the rights-holder(s) directly, unless additional rights are indicated by a Creative Commons license in the record and/or on the work itself.

This Thesis has been accepted for inclusion in UNLV Theses, Dissertations, Professional Papers, and Capstones by an authorized administrator of Digital Scholarship@UNLV. For more information, please contact [digitalscholarship@unlv.edu](mailto:digitalscholarship@unlv.edu).

# POLAR ALIGNMENT OF MASSIVE RETROGRADE CIRCUMBINARY DISCS

By

Charles Abod

Bachelor of Arts - Physics  
Bachelor of Arts - Astrophysics & Planetary Sciences  
University of Colorado, Boulder  
2019

A thesis submitted in partial fulfillment  
of the requirements for the

Master of Science - Astronomy

Department of Physics and Astronomy  
College of Sciences  
Graduate College

University of Nevada, Las Vegas  
August 2022



## Thesis Approval

The Graduate College  
The University of Nevada, Las Vegas

May 24, 2022

This thesis prepared by

Charles Abod

entitled

Polar Alignment of Massive Retrograde Circumbinary Discs

is approved in partial fulfillment of the requirements for the degree of

Master of Science - Astronomy  
Department of Physics and Astronomy

Rebecca Martin, Ph.D.  
*Examination Committee Chair*

Zhaohuan Zhu, Ph.D.  
*Examination Committee Member*

Stephen Lepp, Ph.D.  
*Examination Committee Member*

Laurel Raftery, Ph.D.  
*Graduate College Faculty Representative*

Alyssa Crittenden, Ph.D.  
*Vice Provost for Graduate Education &  
Dean of the Graduate College*

ABSTRACT

**POLAR ALIGNMENT OF MASSIVE RETROGRADE  
CIRCUMBINARY DISCS**

by

Charles Abod

Rebecca Martin, Examination Committee Chair  
Professor of Physics and Astronomy  
University of Nevada, Las Vegas

To understand the observed circumbinary planetary systems, we must first explain the dynamics of the circumbinary discs in which they formed. Observations of circumbinary discs show that misalignments to the binary orbital plane may be common. Here we investigate these systems by exploring the orbital dynamics of three-body systems and circumbinary discs. A test particle orbit around an eccentric binary has two stationary states in which there is no nodal precession: coplanar and polar. Nodal precession of a misaligned test particle orbit centres on one of these stationary states. A low mass circumbinary disc undergoes the same precession and moves towards one of these states through dissipation within the disc. For a massive particle orbit, the stationary polar alignment occurs at an inclination less than  $90^\circ$ , this is the prograde stationary inclination. A sufficiently high angular momentum particle has an additional higher inclination stationary state, the retrograde stationary

inclination. Misaligned particle orbits close to the retrograde stationary inclination are not nested like the orbits close to the other stationary points. We investigate the evolution of a gas disc that begins close to the retrograde stationary inclination. With hydrodynamical disc simulations, we find that the disc moves through the unnested crescent shape precession orbits and eventually moves towards the prograde stationary inclination thus increasing the parameter space over which circumbinary discs move towards polar alignment. This has implications for the alignment of circumbinary planets.

## ACKNOWLEDGEMENTS

I would like to thank Dr. Rebecca Martin for her wonderful guidance and patience through this project and my entire UNLV experience. I would also like to thank Dr. Jeremy Smallwood and Dr. Cheng Chen for providing an amazing foundation for this project. Both in their research, and in their initial coding assistance when I started this project.

I would also like to extend my gratitude to the rest of the Graduate Committee: Dr. Zhaohuan Zhu, Dr. Stephen Lepp, and Dr. Laurel Raftery for their time and patience organizing this defense.

Finally, I would like to thank the amazing friends I made outside of the department: Sam, Kris, Jimmy, Jeffrey, and Edwin. I wouldn't have made it through without their love and support.

Computer support was provided by UNLV's National Supercomputing Center. Support from NASA through grants 80NSSC19K0443 and 80NSSC21K0395 allowed us to pursue this project. This research was supported in part by the National Science Foundation under Grant No. NSF PHY-1748958. Simulations in this paper made use of the REBOUND code. Visualizations of PHANTOM simulations were created through Splash from (Price, 2007).

## TABLE OF CONTENTS

ABSTRACT .....	iii
ACKNOWLEDGEMENTS .....	v
LIST OF TABLES .....	vii
LIST OF FIGURES .....	viii
CHAPTER 1 INTRODUCTION .....	1
CHAPTER 2 THREE-BODY SIMULATIONS .....	6
2.1 Three-body Simulation Set-up .....	6
2.2 Low- $j$ three-Body System.....	12
2.3 Mid- $j$ Three-Body System .....	13
2.4 High- $j$ Three-Body System .....	14
CHAPTER 3 CIRCUMBINARY DISC SIMULATIONS .....	18
3.1 Circumbinary Disc Simulation Set-up .....	18
3.2 Low- $j$ Circumbinary Disc .....	22
3.3 Mid- $j$ Circumbinary Disc .....	24
3.4 High- $j$ Circumbinary Disc .....	27
CHAPTER 4 CONCLUSION .....	29
BIBLIOGRAPHY .....	31
CURRICULUM VITAE .....	37

## LIST OF TABLES

2.1	The initial parameters from the set of three-body and circumbinary disc simulations investigated.....	7
-----	---	---



## LIST OF FIGURES

2.1	Phase and eccentricity plots for the Low- $j$ three-body and circumbinary systems. ....	10
2.2	Phase and eccentricity plots for the Mid- $j$ three-body and circumbinary systems. ....	11
2.3	Visualization graphic that compares the precession paths from a set of the Mid- $j$ three-body systems to their corresponding phase plots. ....	16
2.4	Phase and eccentricity plots for the High- $j$ three-body and circumbinary systems. ....	17
3.1	Visualisation of the Low- $j$ -160 disc-breaking event. ....	19
3.2	The disc mass evolution of all simulations. ....	23
3.3	Phase plot of the Low- $j$ -160 disc-breaking event. ....	25

## CHAPTER 1

### INTRODUCTION

Binary star systems are commonly observed (e.g. Ghez et al., 1993; Duchêne & Kraus, 2013). They are known to form in turbulent molecular clouds (McKee & Ostriker, 2007) where the accretion process may be chaotic (Bate et al., 2003; Bate, 2018). This results in a high likelihood that the protoplanetary disc that forms is misaligned with respect to the orbital plane of the binary (Monin et al., 2007; Bate et al., 2010; Bate, 2018). Circumbinary disc observations suggest that misalignments are common (e.g. Winn et al., 2004; Chiang & Murray-Clay, 2004; Capelo et al., 2012; Brinch et al., 2016; Kennedy et al., 2012; Aly et al., 2018). Circumbinary discs have been observed with polar inclinations of  $90^\circ$  to the binary orbit. HD98800 is a polar circumbinary gas disc (Kennedy et al., 2019) while 99 Her is a polar circumbinary debris disc (Kennedy et al., 2012; Smallwood et al., 2020). The formation and evolution of planets around binaries may be altered by the torque from the binary (e.g. Nelson, 2000; Mayer et al., 2005; Boss, 2006; Martin et al., 2014; Fu et al., 2015a,b, 2017; Franchini et al., 2019). Giant planets that form in a misaligned disc may not remain coplanar to the disc (Picogna & Marzari, 2015; Lubow & Martin, 2016; Martin et al., 2016). We seek to understand the evolution of misaligned circumbinary discs in order to better understand the observed properties of exoplanets.

The Kepler Mission has so far detected about 20 circumbinary planets (e.g. Doyle et al., 2011; Welsh et al., 2012; Orosz et al., 2012; Kostov et al., 2016) and the TESS Mission recently discovered one more (Kostov et al., 2021). All of the circumbinary planets detected so far are nearly coplanar to the binary orbital plane. However, this may be a selection effect due to the small orbital period of the Kepler binaries (Czekala et al., 2019). Longer orbital period binaries are expected to host planets with a wide range of inclinations. Terrestrial circumbinary planets that form through core accretion in the absence of gas may only form in polar or coplanar configurations (Childs & Martin, 2021a,b, 2022), but gas giants that form within the gas disc may form with the same initial inclination as the gas disc (e.g. Pierens & Nelson, 2018). Planets with large misalignments are much more difficult to detect than those that orbit in the binary orbital plane because their transits are much rarer (Schneider, 1994; Martin & Triaud, 2014, 2015; Martin, 2017; Chen & Kipping, 2021). However, other detection methods are possible, such as eclipse timing variations (Murat Esmer et al., 2022). Polar planets (those in an orbit close to perpendicular to the binary orbital plane) may be distinguished from coplanar planets through eclipse timing variations of the binary (Zhang & Fabrycky, 2019). Two circumbinary planets have been found around eccentric orbit binaries. Kepler-34b has a mass of  $0.22M_J$  and orbits an eclipsing binary star system (Kepler-34) that has an orbital eccentricity of 0.52 (Welsh et al., 2012; Kley & Haghighipour, 2015).

The evolution of low mass circumbinary discs is fairly well understood. A misaligned circumbinary disc around a circular orbit binary experiences uniform nodal

precession with constant tilt in the absence of dissipation (e.g. Nixon, 2012; Facchini et al., 2013; Lodato & Facchini, 2013; Foucart & Lai, 2013). The angular momentum vector of the disc precesses about the angular momentum vector of the binary. We call this a *circulating* solution. In this work we focus on protoplanetary discs that are in the wave-like regime in which the disc aspect ratio is much larger than the Shakura & Sunyaev (1973a) viscosity parameter,  $H/R > \alpha$ . For a sufficiently warm and radially narrow disc, the disc precesses as a solid body (e.g. Larwood & Papaloizou, 1997). In these systems, dissipation in the disc leads to alignment with the binary orbital plane (Papaloizou & Terquem, 1995; Lubow & Ogilvie, 2000; Nixon et al., 2011; Nixon, 2012; Facchini et al., 2013; Lodato & Facchini, 2013; Foucart & Lai, 2013, 2014).

The evolution around an eccentric orbit binary is more complex. For a sufficiently high initial tilt, a low mass disc precesses about the eccentricity vector of the binary (rather than the orbital rotation axis of the binary) (Verrier & Evans, 2009; Farago & Laskar, 2010; Doolin & Blundell, 2011; Aly et al., 2015). We call this a *librating* solution, where the orbit is precessing about the *prograde* polar stationary state. In the low mass disc case, the prograde polar stationary state is aligned with the binary eccentricity vector. Dissipation leads to polar alignment where the circumbinary disc is aligned to the eccentricity vector of the binary and perpendicular to the binary orbital plane (Martin & Lubow, 2017; Lubow & Martin, 2018; Zanazzi & Lai, 2018; Martin & Lubow, 2018; Cuello & Giuppone, 2019).

The evolution of a *massive* circumbinary gas disc around an eccentric binary has

not yet been fully explored. In the absence of dissipation within the disc, the dynamical evolution of a radially narrow circumbinary gas disc is qualitatively similar that of a massive particle orbit around the binary. Thus in order to understand the evolution of a massive disc, in Section 2, we first explore the dynamics of massive particle orbits (see also Chen et al., 2019). In this case, the binary feels the gravitational force of the planet which causes the binary orbit to evolve. The eccentricity vector of the binary precesses, the binary orbit tilts and the magnitude of its eccentricity oscillates. The prograde stationary polar aligned state occurs at a lower level of misalignment (Farago & Laskar, 2010; Zanazzi & Lai, 2018; Martin & Lubow, 2019; Chen et al., 2019). For librating orbits, the angular momentum vector precesses around the prograde stationary state. For a gas disc, dissipation causes these oscillations to damp and the disc settles at the prograde stationary tilt angle.

In the massive particle case, there is a third type of nodal precession orbit, that we call the *crescent* orbits. These occur for sufficiently massive particles that begin closer to retrograde than to prograde. These crescent orbits are not nested like the circulating and librating orbits, meaning that they do not have a common centre for the precession. For a sufficiently high angular momentum particle, there is an additional *retrograde* stationary inclination in the region of these crescent orbits. The particle precession in a crescent orbit is not centred around a stationary state. As we show in this paper, a gas disc on such orbits often evolves towards the prograde stationary polar tilt angle. In Section 3 we consider the long term evolution of a gas disc that begins in this regime, close to the retrograde stationary inclination. Finally,

in Section 4, we discuss the implications of our results and state our conclusions.

## CHAPTER 2

### THREE-BODY SIMULATIONS

In this Section, before running our circumbinary disc simulations, we first consider the evolution of a three-body system in order to understand the dynamics of massive circumbinary particle orbits. The parameters we vary are the initial inclination of the third body/planet orbit with respect to the inner binary orbital plane,  $i_0$ , and the angular momentum ratio of the third body compared to the inner binary,  $j$ . Note that in this paper,  $j$  refers to the angular momentum ratio between both planet-binary and disc-binary for the three-body systems and circumbinary disc systems, respectively. For the three-body simulations, we follow the methods outlined in Chen et al. (2019). In Section 3 we compare these results with circumbinary disc simulations which have roughly the same initial parameters,  $j$  and  $i_0$ .

#### 2.1 Three-body Simulation Set-up

We use the  $n$ -body simulation package, REBOUND, with the WHfast integrator which is a second order symplectic Wisdom Holman integrator with 11th order symplectic correctors (Rein & Tamayo, 2015). We solve the gravitational equations for a planet orbiting around a binary star system. The primary mass in the binary is set to be  $M_1 = 0.9 M$ , while the secondary mass is  $M_2 = 0.1 M$ , where  $M = M_1 + M_2$  is

Table 2.1: This table lists the simulation parameters and outcomes. Each line consists of both an  $n$ -body planet simulation and an SPH disc simulation with the same combination of  $j$  and  $i_0$ . The first column describes the simulation name. The second column is the initial inclination of the planet/disc. The third column is the angular momentum ratio of the planet/disc to the binary. The fourth column is the analytically calculated retrograde stationary inclination (see Equation (2.2)). The fifth column is the mass of the planet. The sixth column describes whether the orbit of the planet is retrograde circulating ( $C_R$ ), librating (L) or in a crescent orbit (CRESCENT). The seventh column is the mass of the disc. The eighth column describes the orbit type of the disc prior to its 30% mass loss cut off. The ninth column describes the disc break radius. The tenth column is the time at which the circumbinary disc simulation has lost 30% of its initial mass.

Name	$i_0/^\circ$	$j$	$i_{rs}/^\circ$	$M_p/M$	Planet Orbit	$M_d/M$	Disc Orbit	$R_{\text{Break}}/a_b$	Time ( $T_b$ )
Low- $j$ -120	120	0.5	-	0.006	L	0.01	L	-	2110
Low- $j$ -130	130	0.5	-	0.006	L	0.01	L	-	1540
Low- $j$ -140	140	0.5	-	0.006	L	0.01	L	-	1070
Low- $j$ -150	150	0.5	-	0.006	L	0.01	L	-	850
Low- $j$ -160	160	0.5	-	0.006	L	0.01	L	6	1560
Low- $j$ -170	170	0.5	-	0.006	L	0.01	L	-	2520
Mid- $j$ -100	100	1.5	139	0.018	L	0.03	L	-	2880
Mid- $j$ -110	110	1.5	139	0.018	CRESCENT	0.03	L	-	2320
Mid- $j$ -120	120	1.5	139	0.018	CRESCENT	0.03	CRESCENT $\rightarrow$ L	-	1830
Mid- $j$ -130	130	1.5	139	0.018	CRESCENT	0.03	CRESCENT	-	1410
Mid- $j$ -140	140	1.5	139	0.018	$i_{rs}$	0.03	$i_{rs} \rightarrow$ L	-	1140
Mid- $j$ -150	150	1.5	139	0.018	CRESCENT	0.03	CRESCENT (?)	-	870
Mid- $j$ -160	160	1.5	139	0.018	$C_R$	0.03	$C_R$	2.5	1000
Mid- $j$ -170	170	1.5	139	0.018	$C_R$	0.03	$C_R$	-	2620
High- $j$ -100	100	2.5	129	0.031	L	0.05	L	-	2380
High- $j$ -110	110	2.5	129	0.031	CRESCENT	0.05	CRESCENT $\rightarrow$ L	-	2310
High- $j$ -120	120	2.5	129	0.031	CRESCENT	0.05	CRESCENT	-	2230
High- $j$ -130	130	2.5	129	0.031	$i_{rs}$	0.05	$i_{rs} \rightarrow$ L	-	4200
High- $j$ -140	140	2.5	129	0.031	CRESCENT	0.05	CRESCENT $\rightarrow$ L	-	1980
High- $j$ -150	150	2.5	129	0.031	$C_R$	0.05	$C_R$	-	2020
High- $j$ -160	160	2.5	129	0.031	$C_R$	0.05	$C_R$	2.5	1110
High- $j$ -170	170	2.5	129	0.031	$C_R$	0.05	$C_R$	-	2620

the total mass of the binary. The eccentricity of the binary orbit is set to  $e_b = 0.8$ , and the semi-major axis of the binary is  $a_b$ .

The third body is a planet with mass  $M_p$  that has an initially circular, Keplerian orbit around the centre of mass of the binary. The six orbital elements that define the trajectory of the planet are: its semi-major axis  $a_p$ , inclination  $i$ , eccentricity  $e_p$ , longitude of the ascending node  $\phi$ , argument of periapsis  $\omega$ , and true anomaly  $\nu$ .



Initially we set  $e_p = 0$  and  $\omega = 0$  since the planet’s orbit is initially circular. We also set  $\nu = 0$  and  $\phi = 90^\circ$ . The binary orbit is not fixed and can feel the gravity of the orbiting planet. Therefore, to remove the chance of running into orbital instability, we follow Chen et al. (2019) and choose a relatively large semi-major axis of the planet of  $a_p = 20 a_b$ , where the orbits are stable for all inclinations (Chen et al., 2020a). Consequently, this increases the time required to complete the three-body simulations, which we take to be  $6000 T_b$ , where the binary orbital period is  $T_b$ . . We define  $j$  to be the planet-to-binary angular momentum ratio. For our three-body simulations,  $j = J_p/J_b$ , where  $J_p$  is the angular momentum of the orbiting planet and  $J_b$  is the angular momentum of the binary. We vary the planet mass to give the required value for  $j$ . Note that the system dynamics depend only on the angular momentum ratio  $j$  and the binary eccentricity  $e_b$  (Martin & Lubow, 2019). We probe systems with three different  $j$  values, each with a set of different initial inclinations,  $i_0$ , see Table 2.1. The planet’s orbit remains approximately circular throughout the simulations, as is expected analytically since the particle eccentricity is a constant of motion in the secular quadrupole approximation for the binary (Farago & Laskar, 2010).

The stationary inclinations for the test particle occur when the particle orbit displays no precession with respect to the binary. These can be calculated analytically with

$$\cos i = \frac{-(1 + 4e_b^2) \pm \sqrt{(1 + 4e_b^2)^2 + 60(1 - e_b^2)j^2}}{10j} \quad (2.1)$$

(Martin & Lubow, 2019; Chen et al., 2019). (Note that there is a typo in Equation 5 in Chen et al. (2019).) We take the positive sign to calculate the prograde stationary inclination,  $i_s$ . This is the centre of the librating region. We take the negative sign in Equation (2.1) to calculate the retrograde stationary inclination  $i_{rs}$ . But, this only exists if the angular momentum ratio is greater than the critical value of

$$j_{\text{cr}} = \frac{1 + 4e_b^2}{2 + 3e_b^2} \quad (2.2)$$

(see Appendix A of Martin & Lubow, 2019). For the binary eccentricity of  $e_b = 0.8$  considered in this work,  $j_{\text{cr}} = 0.91$ .

Given this value of  $j_{\text{cr}}$ , we set our "low", "middle", and "high" values to be  $j = 0.5, 1.5$ , and  $2.5$  respectively. We chose these values to probe above and below  $j_{\text{cr}}$ . We choose two values greater than  $j_{\text{cr}} = 0.91$  to further investigate the parameter regime where crescent orbits are found. We increase the initial angular momentum ratio between the planet and binary by increasing the planet mass. The angular momentum ratio is given by

$$j = \frac{\frac{M_p}{M} \sqrt{\frac{a_p}{a_b}} \sqrt{1 + \frac{M_p}{M}}}{f_b(1 - f_b)\sqrt{1 - e_b^2}}, \quad (2.3)$$

where  $f_b = M_1/M_2$  is the binary mass fraction. We solve this for  $M_p$  values that are associated with  $j = 0.5, 1.5$ , and  $2.5$  and the values are shown in Table 2.1.

We work in a frame defined by the instantaneous values of the binary eccentricity

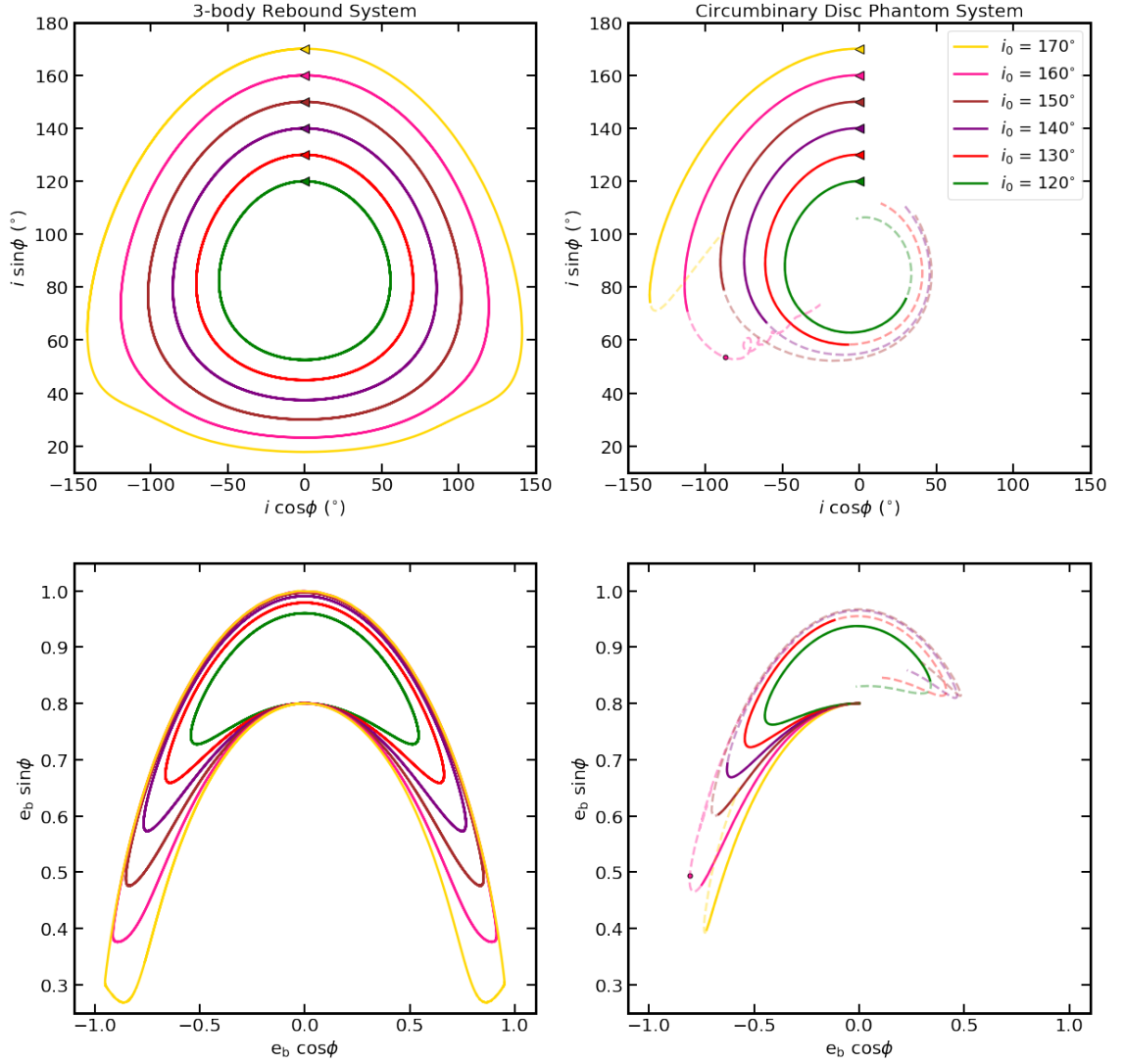


Figure 2.1: The top two panels show the  $i \cos \phi - i \sin \phi$  phase plot of the planet (left) and disc (right). The bottom two plots show the  $e_b \cos \phi - e_b \sin \phi$  plane of the binary stars for the three-body system (left) and the circumbinary disc system (right). The dashed lines represent any part of the system that is simulated past the point where the disc has lost 30% of its initial mass (see Fig. 3.2). All simulations, both disc and planet, have  $j = 0.5$  initially. The three-body system has a planet with mass  $M_p = 0.006 M$  and initial planet distance from system centre of mass of  $r = 20 a_b$ . The initial mass of the disc is  $M_d = 0.01 M$ . Additionally, the pink dot on each of the right plots indicates the point where that circumbinary disc broke apart at time  $T = 2600 T_b$ .

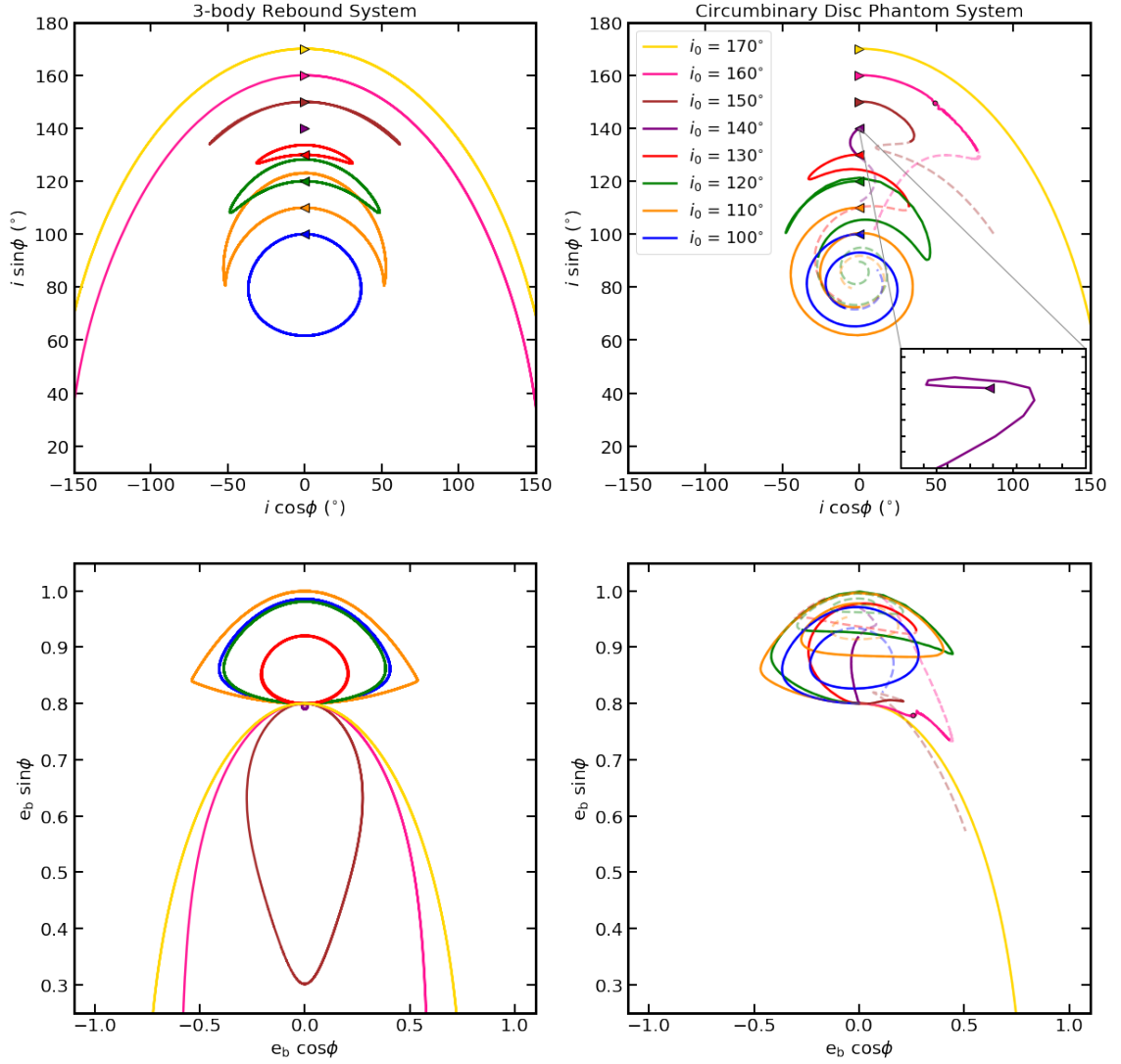


Figure 2.2: Same as Fig. 2.1 except  $j = 1.5$ . The three-body systems have a planet with mass  $M_p = 0.018 M$  and initial planet distance from system centre of mass  $r = 20 a_b$ . The initial mass of the disc is  $M_d = 0.03 M$ . Additionally, the pink dot on each of the right plots indicates the point where that circumbinary disc broke apart at  $T = 240 T_b$ .

vector,  $\mathbf{e}_b$ , and angular momentum vector,  $\mathbf{l}_b$ . The binary frame has three axes  $\mathbf{e}_b$ ,  $\mathbf{l}_b$ , and  $\mathbf{l}_b \times \mathbf{e}_b$ . The inclination of the planet's orbital plane relative to the binary orbital plane is

$$i = \cos^{-1}(\hat{\mathbf{l}}_b \cdot \hat{\mathbf{l}}_p), \quad (2.4)$$

where the planet’s angular momentum vector is  $\mathbf{l}_p$  and  $\hat{\cdot}$  denotes a unit vector. The nodal phase angle of the planet is

$$\phi = \frac{\pi}{2} + \tan^{-1} \left( \frac{\hat{\mathbf{l}}_p \cdot (\hat{\mathbf{l}}_b \times \hat{\mathbf{e}}_b)}{\hat{\mathbf{l}}_p \cdot \hat{\mathbf{e}}_b} \right) \quad (2.5)$$

(Chen et al., 2019, 2020b). In the following subsections, we explore the planet orbits produced from the three initial angular momentum ratio systems, each with their set of initial inclinations.

## 2.2 Low- $j$ three-Body System

We first consider three-body simulations with a relatively low third body angular momentum of  $j = 0.5 < j_{\text{cr}} = 0.91$ . The prograde stationary inclination calculated with Equation (2.1) is  $i_s = 82^\circ$ . There is no retrograde stationary inclination in this case since the angular momentum ratio is lower than the critical defined by Equation (2.2). The two left panels in Fig. 2.1 show the results of the Low- $j$  three-body simulations. The top left plot shows the inclination phase plot,  $i \cos \phi - i \sin \phi$ . In this low mass case, all of the orbits shown in the phase plot are librating, meaning the particle angular momentum vector is precessing about the generalised polar inclination. All of the orbits begin at their respective initial inclinations and carry out their paths in a counterclockwise direction. The coloured triangle is located at the start of the path and points to the initial direction. The lower left panel shows the eccentricity phase plot  $e_b \cos \phi - e_b \sin \phi$ . All of the results in the eccentricity phase plot begin

at  $e_b = 0.8$ , and  $\sin \phi = 1$  and carry out their paths in a clockwise direction. In all cases, the binary eccentricity oscillates and initially increases from its initial value.

### 2.3 Mid- $j$ Three-Body System

We now consider a more massive planet such that the angular momentum ratio  $j = 1.5 > j_{\text{cr}} = 0.91$ . The prograde stationary inclination calculated with Equation (2.1) is  $i_s = 73^\circ$  and the retrograde stationary inclination is  $i_{\text{rs}} = 139^\circ$ . The left two panels of Fig. 2.2 show the results of the Mid- $j$  three-body simulations. The top phase plot shows that for initial inclination  $i_0 \lesssim 100^\circ$ , the orbit is librating about the prograde stationary inclination. For  $i_0 \gtrsim 160^\circ$ , the orbits are in retrograde circulation, meaning that the planet angular momentum vector is precessing about the negative of the binary angular momentum vector. In the approximate initial inclination range,  $110^\circ - 150^\circ$  we see crescent orbits. These crescent orbits are not nested on a common centre like the circulating or librating orbits. The Mid- $j$ -140 three-body simulation does not show significant variation from its initial inclination in the phase plot because of its proximity to the retrograde stationary inclination at  $i_{\text{rs}} = 139^\circ$ . Additionally, as seen by the coloured triangles, the three-body systems with  $i_0 < i_{\text{rs}}$  precess counterclockwise, while those with  $i_0 > i_{\text{rs}}$  precess clockwise.

Looking at the lower left panel Fig. 2.2 in we see that the binary eccentricity oscillates in all cases, but the initial direction varies depending upon the initial inclination. If  $i_0 < i_{\text{rs}}$ , then the eccentricity initially increases, while for  $i_0 > i_{\text{rs}}$ , the eccentricity initially decreases. The initial horizontal direction of the paths in the

inclination phase plot correlates with the initial vertical direction of the eccentricity plots. The orbital paths that have rightward-facing triangles have an initially decreasing  $e_b$ , while orbits with leftward-facing triangles have an initially increasing  $e_b$ .

To better understand what the phase plots represent in three-dimensions, Fig. 2.3 connects the angular momentum evolution to the phase plots in Fig. 2.2. From this depiction, we are able to see the true shapes of these orbital paths without the alterations that are made when mapping the spherical path onto a Cartesian coordinate system.

## 2.4 High- $j$ Three-Body System

We now consider our most massive planet with the highest angular momentum ratio,  $j = 2.5 > j_{\text{cr}} = 0.91$ . The prograde stationary inclination calculated with Equation (2.1) is  $i_s = 70^\circ$ , and the retrograde stationary inclination is  $i_{\text{rs}} = 129^\circ$ . The left two panels of Fig. 2.4 show the results of these High- $j$  three-body simulations. The phase plot behaviour is similar to the Mid- $j$  simulations, but with some of the orbital phenomenon shifted downwards by about  $10^\circ$ . For  $i_0 \lesssim 100^\circ$ , the orbit is librating about  $i_s$ . For  $i \gtrsim 150^\circ$ , the orbits are in retrograde circulation. We find the crescent orbit regime to be approximately within  $110^\circ - 140^\circ$ . Similar to the behaviour of Mid- $j$ -140, we find that High- $j$ -130 does not deviate significantly from its initial inclination due to its proximity to the retrograde stationary inclination at  $i_{\text{rs}} = 139^\circ$ . When looking at the eccentricity plots we find the similar behaviours as

described in Sec. 2.3.



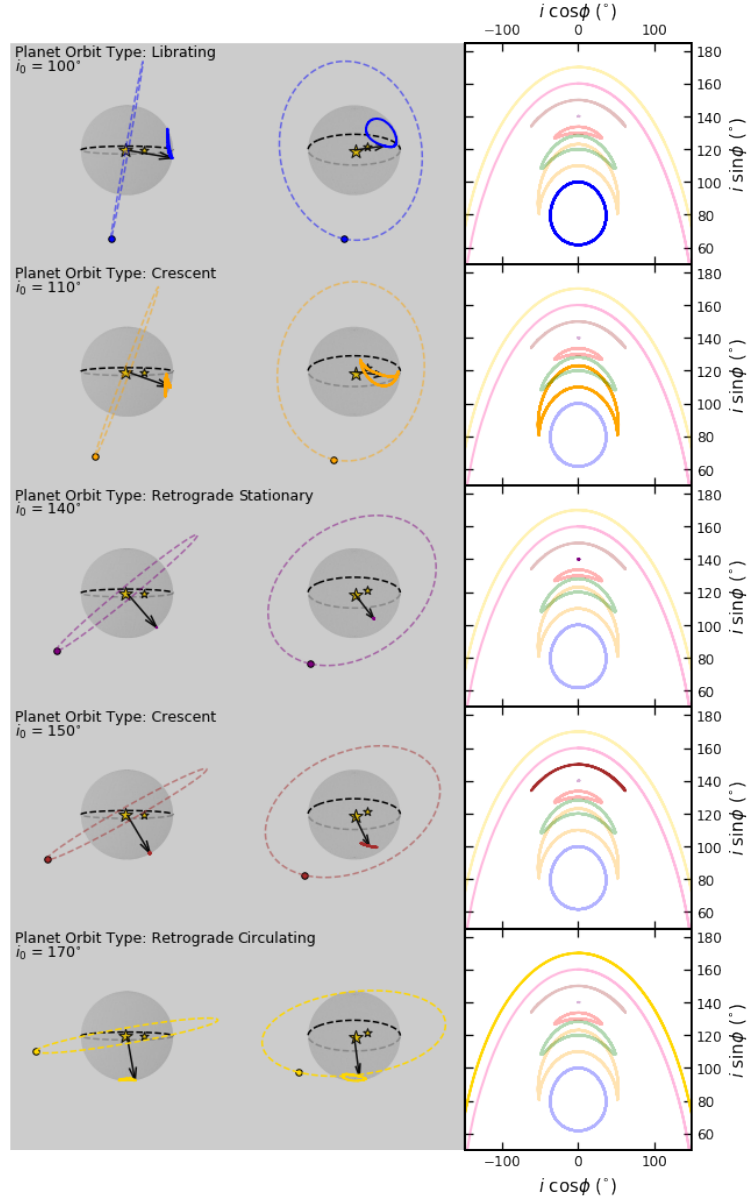


Figure 2.3: Precession paths in 3D for the Mid- $j$  simulations. Each row corresponds to a different initial inclination,  $i_0$ , that is highlighted in the inclination phase plot on the right that is the same as the upper left panel in Fig. 2.2. The left and middle columns show 3D visual representations of the three-body simulations. The left column is viewed from azimuth =  $0^\circ$  and elevation =  $-5^\circ$ , while the middle column is viewed from azimuth =  $50^\circ$  and elevation =  $-20^\circ$ . The two yellow stars in the centre are the binary stars that are shown at apastron, the dotted coloured line and circle outside of the gray sphere are the third body with its trajectory, the black arrow is the angular momentum vector of the third body, and the solid coloured line on the sphere is the path of the planet's angular momentum vector for a complete precession. The black and grey dotted lines on the sphere show the plane in which the binary orbits.

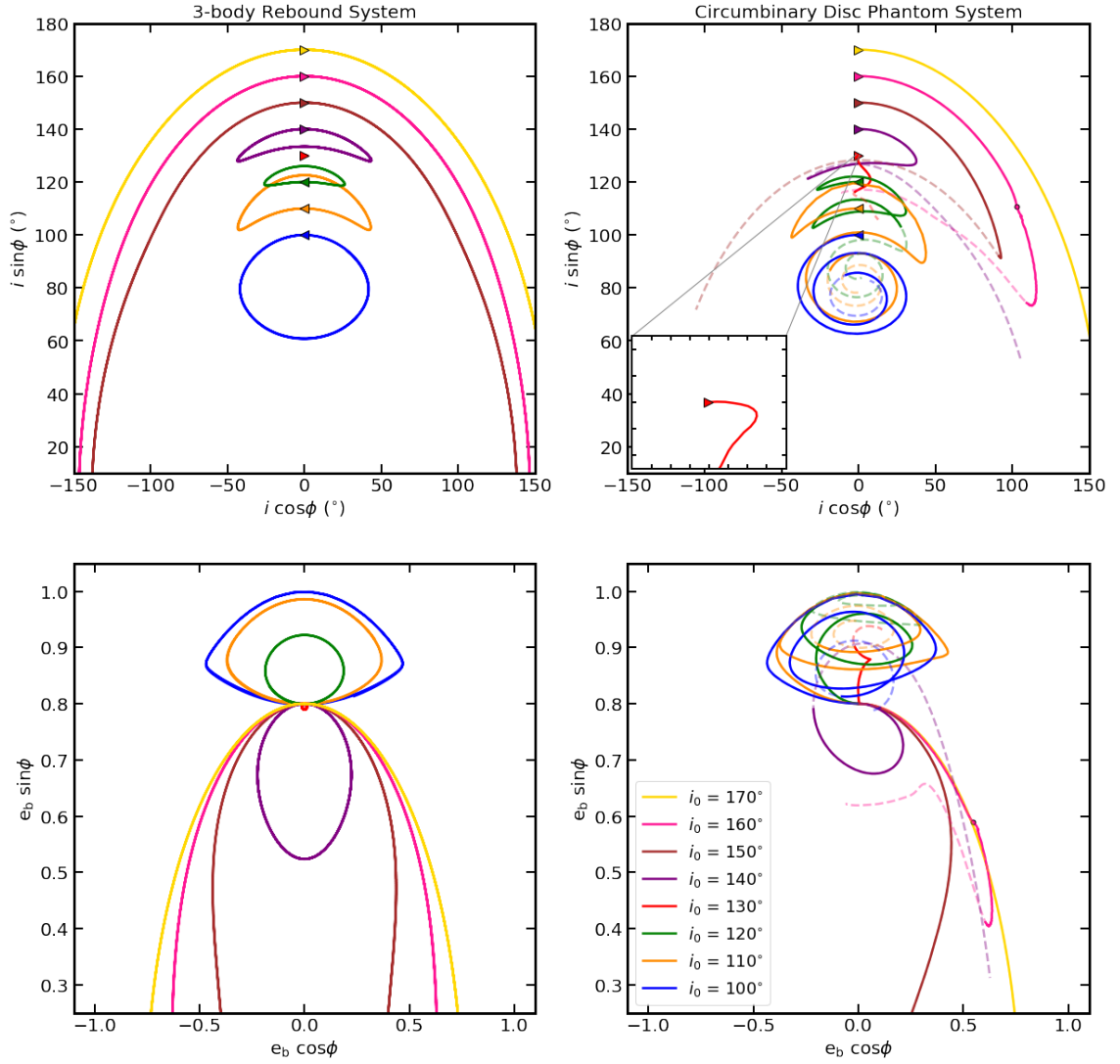


Figure 2.4: Same as for 2.1 except  $j = 2.5$ . The three-body systems have a planet mass  $M_p = 0.031 M$  and initial planet distance from system centre of mass  $r = 20 a_b$ . The initial mass of the disc is  $M_d = 0.05 M$ .

## CHAPTER 3

### CIRCUMBINARY DISC SIMULATIONS

In this section, we explore hydrodynamical simulations of a circumbinary gas disc with the same initial properties ( $i_0$  and  $j$ ) as the three-body simulations in the previous Section in order to understand the long term evolution of a massive circumbinary disc.

#### 3.1 Circumbinary Disc Simulation Set-up

We use the smoothed particle hydrodynamics (SPH) code PHANTOM (Price & Federrath, 2010; Price et al., 2018) to simulate circumbinary discs. The binary and disc parameters have the same initial inclination and angular momentum as the three-body simulations in the previous Section. We define the angular momentum ratio as  $j = J_d/J_b$ , where  $J_d$  is the angular momentum of the disc. All discs start with surface density distributed with a power law  $\Sigma \propto R^{-3/2}$  between the initial inner disc radius  $R_{\text{in},0} = 5 a_b$  and the initial outer radius  $R_{\text{out},0} = 10 a_b$ . The initial inner disc truncation radius is chosen to be initially far from the binary so that the disc expands beyond the initial inner and outer radii. We take the Shakura & Sunyaev (1973b)  $\alpha$  parameter to be 0.01 in all of our simulations. This disc viscosity is utilized by adapting the SPH artificial viscosity according to Lodato & Price (2010). The disc

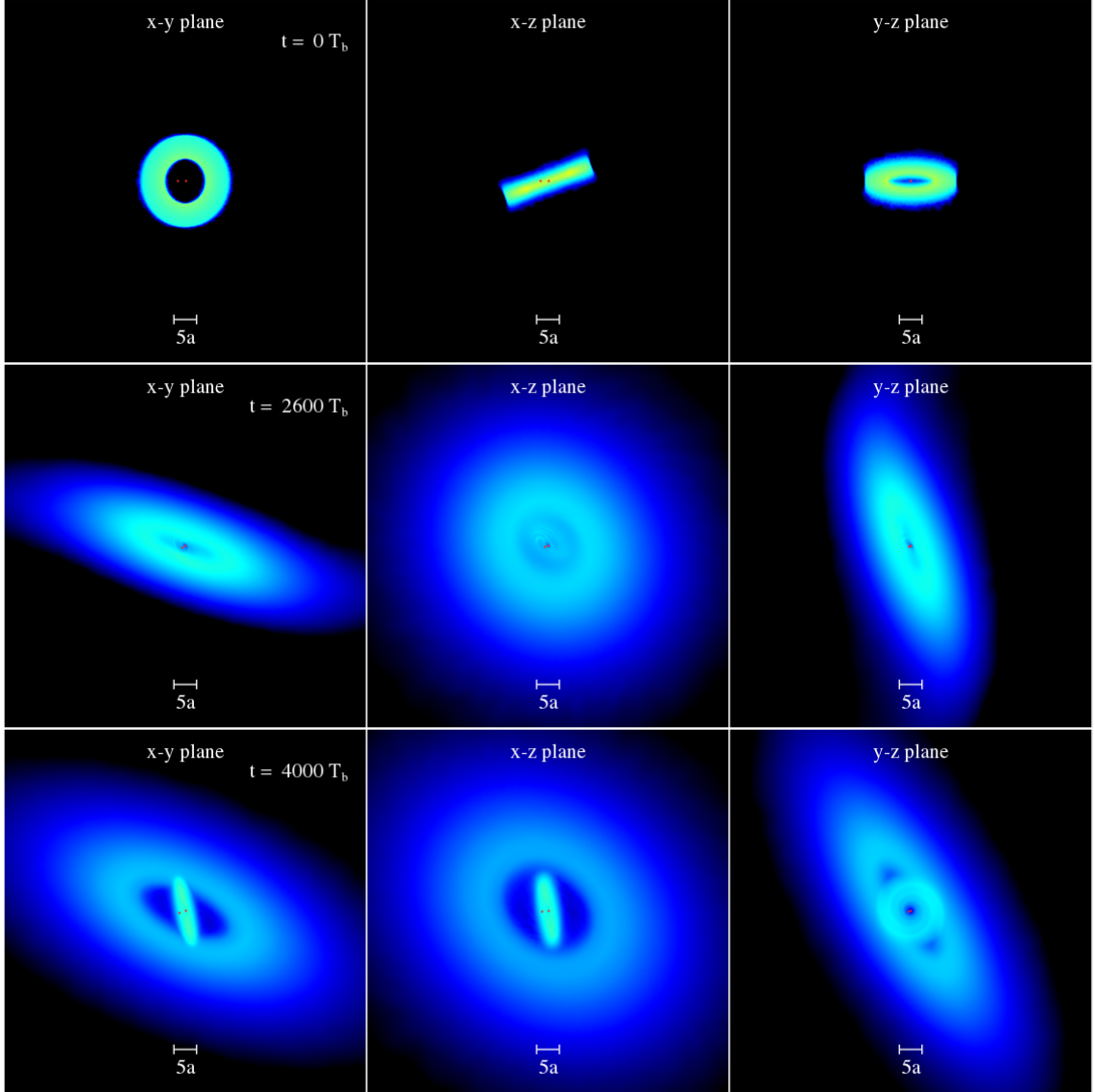


Figure 3.1: Snapshots from the Low- $j$ -160 broken-disc system. The top row shows the initial conditions of the circumbinary disc from three different viewing angles. The middle row shows the time where we classify the disc as broken and begin analysing the data from the inner and outer disc separately. Note that  $t = 2600 T_b$  is where the red and blue lines meet in Fig. 3.3. The bottom row shows the simulation at a later time where the two discs are fully separated, and the inner disc has gone nearly polar.

is locally isothermal with sound speed  $c_s \propto R^{-3/4}$  and the disc aspect ratio varies with radius as  $H/R \propto R^{-1/4}$ . Thus,  $\alpha$  and the average smoothing length  $\langle h \rangle / H$

are constant over the radial extent of the disc (Lodato & Pringle, 2007). We take  $H/R = 0.1$  at  $R_{\text{in}}$ . Particles from the disc are removed if they pass inside the accretion radius for each component of the binary at  $0.25 a_{\text{b}}$  (Bate et al., 1995). We run our disc simulations with  $1 \times 10^6$  particles initially. The disc is initially resolved with averaged smoothing length divided by the disc scale height of  $\langle h \rangle / H = 0.15$ . We have simulations with three disc masses  $M_{\text{d}} = 0.01 M$ ,  $0.03 M$ , and  $0.05 M$ . We run these simulations up until  $t = 6000 T_{\text{b}}$ , except for Low- $j$ -170, Mid- $j$ -140, Mid- $j$ -150, High- $j$ -130, High- $j$ -140, and High- $j$ -150 which are run until  $t = 10000 T_{\text{b}}$ . However, we indicate the time at which the disc has lost 30% of its initial mass in both our figures and tables. Beyond this time, the comparison to the equivalent three-body simulations may not be appropriate. The time is shown in the final column in Table 2.1.

One detriment to note in our SPH simulations is that the flow in the central gap region is not well resolved by the code in the intrinsically 3D flows. That flow takes the form of rapid low density gas streams (e.g. Artymowicz & Lubow, 1996; Muñoz et al., 2019; Mösta et al., 2019). This causes some uncertainty in the binary evolution.

In order to analyse the properties of the disc, we divide the disc up into 10000 bins in spherical radius up to a radius of  $R_{\text{out}} = 100 a_{\text{b}}$ . Within each bin we average the orbital properties of the particles, such as the inclination,  $i$ , and nodal phase angle,  $\phi$ . Similar to the three-body simulations, we compute the inclination of a ring of the

disc at radius  $R$  relative to the instantaneous binary angular momentum as

$$i(R) = \cos^{-1} \left( \hat{\mathbf{l}}_{\text{b}} \cdot \hat{\mathbf{l}}_{\text{d}}(R) \right), \quad (3.1)$$

where  $\hat{\mathbf{l}}_{\text{d}}(R)$  is the unit vector in the direction of the disc angular momentum vector.

We then calculate the inclination of the disc as the density weighted average of the inclination

$$i = \frac{\int_{R_{\text{in}}}^{R_{\text{out}}} 2\pi i(r) r \Sigma(r) dr}{M_{\text{tot}}}, \quad (3.2)$$

where  $\Sigma(R)$  is the surface density at radius  $R$ ,  $i(R)$  is the inclination at radius  $R$ , and  $M_{\text{tot}}$  is the total mass of the disc at the given time. The longitude of the ascending node phase angle for the disc is

$$\phi(R) = \tan^{-1} \left( \frac{\hat{\mathbf{l}}_{\text{d}}(R) \cdot (\hat{\mathbf{l}}_{\text{b}} \times \hat{\mathbf{e}}_{\text{b}})}{\hat{\mathbf{l}}_{\text{d}}(R) \cdot \hat{\mathbf{e}}_{\text{b}}} \right). \quad (3.3)$$

In a similar fashion to  $i$ ,  $\phi$  for the disc is also a density weighted average of the particles in the disc with

$$\phi = \frac{\int_{R_{\text{in}}}^{R_{\text{out}}} 2\pi \phi(r) r \Sigma(r) dr}{M_{\text{tot}}}. \quad (3.4)$$

In the following Sections, we discuss the results of our circumbinary disc simulations in relation to their corresponding three-body system results.

### 3.2 Low- $j$ Circumbinary Disc

Here we describe the Low- $j$  hydrodynamical simulations of circumbinary discs, where  $j = 0.5 < j_{\text{cr}} = 0.91$ . The right two plots of Fig. 2.1 show the orbital phase and eccentricity results of these systems. The top right plot shows the  $i \cos \phi - i \sin \phi$  plane and the lower right plot shows the eccentricity phase plot  $e_b \cos \phi - e_b \sin \phi$ . When compared to the equivalent three-body system (left), we see general agreement in the phase plots for  $i_0 \lesssim 160^\circ$ . While the three-body orbits are exactly periodic, the disc simulations include dissipation which causes the disc to gradually align toward the prograde stationary inclination in a spiral-like motion. The upper panel of Fig. 3.2 shows the mass of each disc in time. The lines are dashed after the disc mass has lost 30% of the initial value. This corresponds to the dashed lines in the phase plots in Fig. 2.1.

The higher initial inclinations, where  $i \gtrsim 160^\circ$ , show somewhat different behaviour. For Low- $j$ -160, the disc initially follows a similar evolution to the particle, but then begins to move quickly towards polar alignment. This behaviour can be seen in the pink line in Fig. 2.1 which experienced a disc break at a time of  $t = 2600 T_b$ . The disc breaks into two disjoint rings at a break radius of around  $R = 6 a_b$ . This is visually displayed in Fig. 3.1. Disc breaking occurs when the radial communication in the disc occurs on a longer timescale than the precession timescale (Papaloizou & Terquem, 1995; Larwood et al., 1996; Nixon et al., 2013). Protoplanetary discs are typically in the wave-like regime since  $H/R \gg \alpha$  (Papaloizou & Pringle, 1983) and bending waves, that propagate at about half the sound speed, communicate the warp

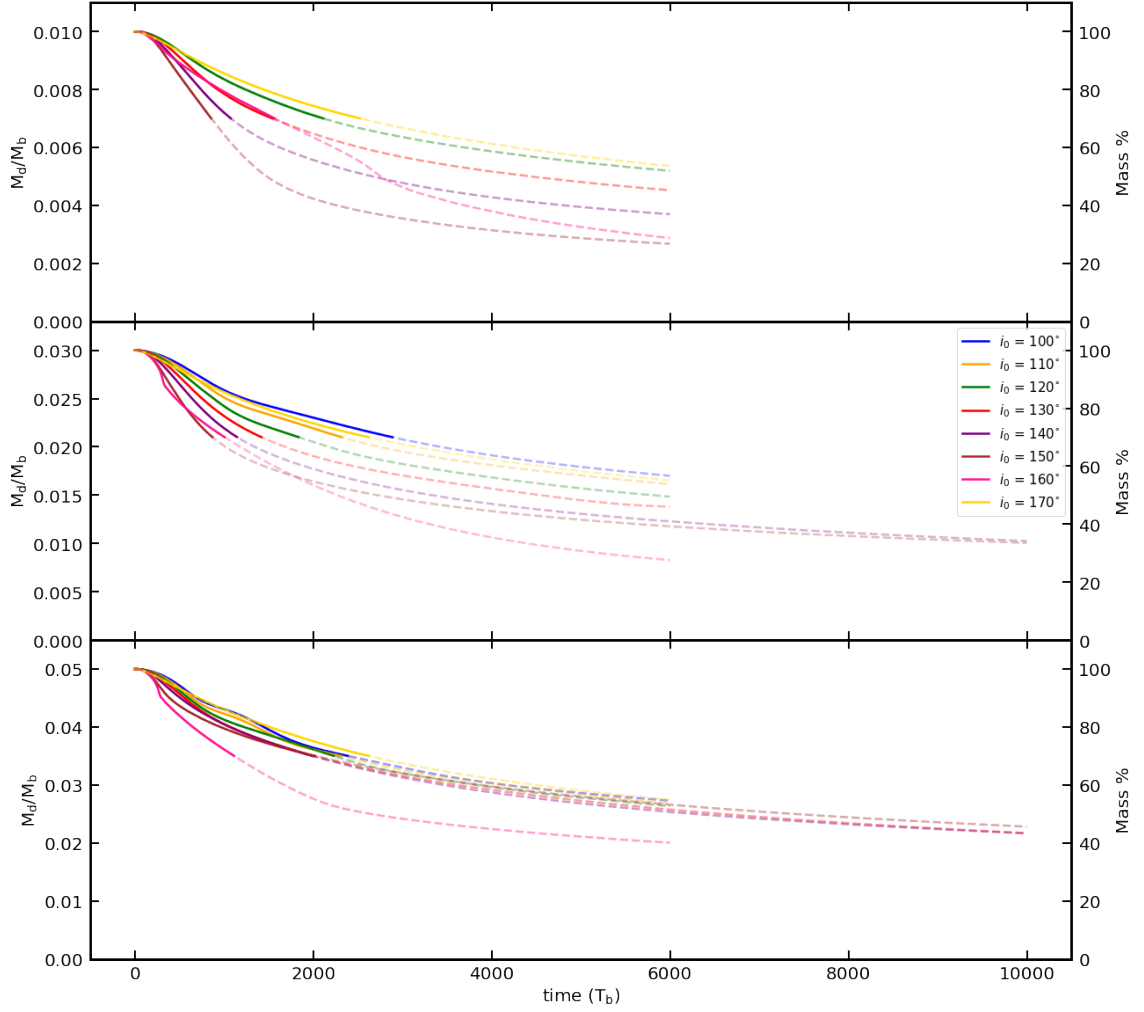


Figure 3.2: The disc mass evolution of all simulations. The dashed lines represent where each simulation has lost more than 30% of its initial mass.

(Papaloizou & Terquem, 1995). Also, Fig. 3.3 shows the inclination phase plot for just this simulation. The pink line here is the same as in the upper right panel of Fig. 2.1. The blue and red lines show the inner and outer disc respectively plotted. The inner disc is analysed at  $R = 5 a_b$ , while the outer disc is set at  $R = 25 a_b$ . The outer disc continues much on the original path, while the inner disc quickly spirals to polar. The combination of these two paths is why we observe a sharp, but looping



path towards polar alignment. As seen in Fig. 3.1, the radius of the disc break grows over time. Thus, the inclination of the total disc is dominated by the inclination of the inner disc at larger times.

Similar to the three-body paths, we find that the initial direction of the orbital paths (denoted with the coloured triangles) corresponds with the initial direction of the eccentricity plots. The orbital paths with rightward-facing triangles have an initially decreasing  $e_b$ .

### 3.3 Mid- $j$ Circumbinary Disc

The right two panels of Fig. 2.2 show the phase plots of the Mid- $j$  circumbinary disc simulations with  $j = 1.5 > j_{\text{cr}} = 0.91$ . When compared to the equivalent Mid- $j$  three-body systems (left), we see general agreement for the highest inclination case of the Mid- $j$ -170 system. For  $i_0 \lesssim 110^\circ$ , we see librating precession and the disc spirals towards polar alignment. The Mid- $j$ -110 system in the three-body case shows a crescent orbit but this is not seen for the disc. However, in the approximate range of  $120^\circ - 150^\circ$ , the disc begins at first on a crescent type orbit. In this range, the disc moves towards libration and polar alignment. For Mid- $j$ -120 and Mid- $j$ -130, we see at least one complete phase of a crescent orbit before the disc begins librating. It is important to note that some of these transitions into librating orbits occur after the disc has lost more than 30% of its initial mass, and thus direct comparison to the three-body system shown may not be applicable. The value for the angular momentum ratio  $j$  is decreasing during the simulation because mass is lost from the

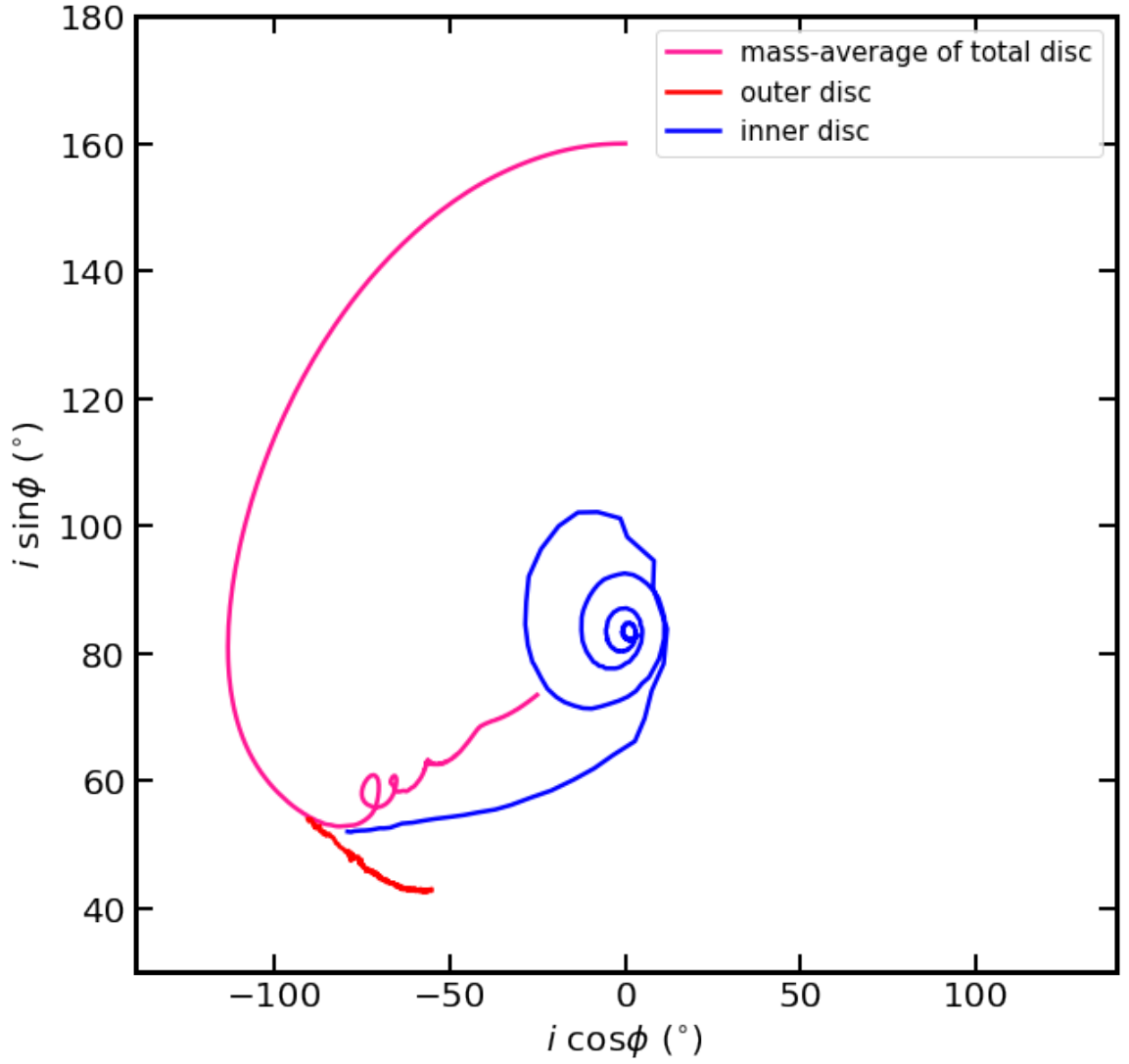


Figure 3.3: The  $i \cos \phi - i \sin \phi$  phase plot for the Low- $j$ -160 broken disc. The blue line represents the inner disc at  $R = 5 a_b$ , while the red line represents the outer disc, set at  $R = 25 a_b$  after the disc has broken at time of  $t = 2600 T_b$ . The pink line is the same pink line shown in Fig. 2.1.

disc and accreted on to the binary (see the middle panel of Fig. 3.2). However, for the Mid- $j$ -120 simulation, the mass remains high while the orbit transitions to libration.

For Mid- $j$ -140 and Mid- $j$ -150, we observe the beginning of a descent to polar alignment which differs greatly from the respective three-body simulations. Note that Mid- $j$ -140 begins very close to the retrograde stationary inclination  $i_{\text{rs}}$  and we see that the initial direction of this orbital path is opposite to that of the respective three-body orbit. We find that most initial inclinations seem to ignore the retrograde stationary inclination  $i_{\text{rs}}$  in order to evolve towards a librating orbit around polar alignment  $i_{\text{s}}$ .

Finally, for  $i = 160^\circ$  we again observe the disc breaking at a time of  $t = 300 T_{\text{b}}$ . We can see the moment of the disc break in the pink inclination and eccentricity paths where there is a small bump and pink dot to indicate the time of the disc break. The approximate radius of this disc break was at  $R = 2.5 a_{\text{b}}$ .

For  $i \lesssim 130^\circ$ , we find that the initial direction of the orbital paths, denoted with the coloured triangles, corresponds with the initial direction of the eccentricity plots. However, for Mid- $j$ -140 and Mid- $j$ -150 we find the eccentricities initially increasing unlike their respective three-body paths. For Mid- $j$ -160, we see an initial decrease followed by an increase in a counter-clockwise rotation unlike the clockwise rotation in the three-body path. For Mid- $j$ -170, we see general agreement with both the eccentricity and inclination phase plots.

### 3.4 High- $j$ Circumbinary Disc

Here we describe simulations of circumbinary discs with  $j = 2.5 > j_{\text{cr}} = 0.91$ . The right two plots of Fig. 2.4 show the results of the High- $j$  circumbinary disc simulations. When compared to the equivalent three-body system, we see general agreement for only the  $i_0 = 100^\circ$  and  $i_0 = 170^\circ$  systems. For High- $j$ -100, we see a librating orbit spiraling towards polar alignment. For High- $j$ -110 and High- $j$ -120, we see at least one phase of crescent orbits that descend into librating orbits around polar alignment. While High- $j$ -120 has lost a significant amount of mass before it begins librating, High- $j$ -110 has not (see the lower panel of Fig. 3.2). Specifically for High- $j$ -120, we see at least two crescent orbits before descending to polar libration. For High- $j$ -130, we observe the beginning of a descent to polar alignment which differs greatly from the respective three-body simulation. Note that High- $j$ -130 is the closest to the retrograde stationary inclination  $i_{\text{rs}}$  for  $j = 2.5$ , and we see that the initial direction of this orbital path is opposite to the respective three-body simulation.

For  $i \lesssim 120^\circ$ , we find that the initial direction of the orbital paths (denoted with the coloured triangles) corresponds with the initial direction of the eccentricity plots (as discussed in Section 2.4). The High- $j$ -140 and High- $j$ -150 eccentricities initially decrease like their respective three-body paths. For High- $j$ -160, we see an initial decrease followed by an increase in a counter-clockwise rotation unlike the clockwise rotation in the three-body path. This behaviour can be seen in the pink line in Fig. 2.1 which this system also experienced a disc break at a time of  $t = 270 T_{\text{b}}$ . The disc breaks into two disjoint rings at a break radius of around  $R = 2.5 a_{\text{b}}$ . For High- $j$ -170,

we see general agreement with both the eccentricity and inclination phase plots.

## CHAPTER 4

### CONCLUSION

We have investigated the evolution of a massive circumbinary disc that begins with an inclination that is closer to retrograde alignment than prograde alignment to the binary orbit. We have found that at least initially a circumbinary disc displays similar behaviour to a three-body simulation with the same angular momentum ratio of the outer body to the inner binary. Dissipation and radial communication across the disc lead to differences later on. For a narrow range of initial disc inclinations around  $i = 160^\circ$  the disc communication timescale is longer than the nodal precession timescale and this leads to breaking, where the disc has two disjoint rings that can precess independently. Qualitatively the behaviour is not affected by the disc break.

With three-body simulations we have explored the dynamics of a massive third body orbiting an eccentric binary. There are three different types of nodal precession for massive bodies. First, the third body may be circulating, meaning that it precesses about the binary angular momentum vector (prograde circulation) or the negative of the binary angular momentum vector (retrograde circulation). Second, if the initial inclination is close to the generalised stationary inclination, it may be librating, meaning that it precesses about the generalised polar state. For inclinations between the retrograde circulation and the libration, the particle may be in a crescent

type orbit in the inclination phase plot. These orbits do not have a common centre. There are two stationary inclinations for which there is no nodal precession of the orbit. The prograde stationary inclination lies at the centre of the librating orbits. The retrograde stationary inclination exists for sufficiently high angular momentum of the third body and lies within the crescent orbits.

We have found that the dissipation within the circumbinary disc leads to polar alignment for all orbits that begin in the crescent orbit regime. Even if a disc begins very close to the retrograde stationary inclination, it does not stay there. This means that the phase space for which a retrograde disc moves towards polar alignment is larger than would be predicted by just the librating orbits. A massive and close to retrograde circumbinary disc eventually moves towards the prograde stationary inclination. This result has implications for the formation of planets around an eccentric orbit binary since polar discs may form from a wide range of initial disc misalignments.

## BIBLIOGRAPHY

Aly H., Dehnen W., Nixon C., King A., 2015, MNRAS, 449, 65

Aly H., Lodato G., Cazzoletti P., 2018, MNRAS, 480, 4738

Artymowicz P., Lubow S. H., 1996, ApJ, 467, L77

Bate M. R., 2018, MNRAS, 475, 5618

Bate M. R., Bonnell I. A., Price N. M., 1995, MNRAS, 277, 362

Bate M. R., Bonnell I. A., Bromm V., 2003, MNRAS, 339, 577

Bate M. R., Lodato G., Pringle J. E., 2010, MNRAS, 401, 1505

Boss A. P., 2006, ApJ, 641, 1148

Brinch C., Jørgensen J. K., Hogerheijde M. R., Nelson R. P., Gressel O., 2016, ApJ, 830, L16

Capelo H. L., Herbst W., Leggett S. K., Hamilton C. M., Johnson J. A., 2012, ApJ, 757, L18

Chen Z., Kipping D., 2021, arXiv e-prints, p. arXiv:2112.00966

Chen C., Franchini A., Lubow S. H., Martin R. G., 2019, MNRAS, 490, 5634



- Chen C., Lubow S. H., Martin R. G., 2020a, MNRAS, 494, 4645
- Chen C., Franchini A., Lubow S. H., Martin R. G., 2020b, MNRAS, 495, 141
- Chiang E. I., Murray-Clay R. A., 2004, ApJ, 607, 913
- Childs A. C., Martin R. G., 2021a, MNRAS, 507, 3461
- Childs A. C., Martin R. G., 2021b, ApJ, 920, L8
- Childs A. C., Martin R. G., 2022, ApJ, 927, L7
- Cuello N., Giuppone C. A., 2019, A&A, 628, A119
- Czekala I., Chiang E., Andrews S. M., Jensen E. L. N., Torres G., Wilner D. J.,  
Stassun K. G., Macintosh B., 2019, ApJ, 883, 22
- Doolin S., Blundell K. M., 2011, MNRAS, 418, 2656
- Doyle L. R., et al., 2011, Science, 333, 1602
- Duchêne G., Kraus A., 2013, ARA&A, 51, 269
- Facchini S., Lodato G., Price D. J., 2013, MNRAS, 433, 2142
- Farago F., Laskar J., 2010, MNRAS, 401, 1189
- Foucart F., Lai D., 2013, ApJ, 764, 106
- Foucart F., Lai D., 2014, MNRAS, 445, 1731
- Franchini A., Martin R. G., Lubow S. H., 2019, MNRAS, 485, 315

- Fu W., Lubow S. H., Martin R. G., 2015a, ApJ, 807, 75
- Fu W., Lubow S. H., Martin R. G., 2015b, ApJ, 813, 105
- Fu W., Lubow S. H., Martin R. G., 2017, ApJ, 835, L29
- Ghez A. M., Neugebauer G., Matthews K., 1993, AJ, 106, 2005
- Kennedy G. M., et al., 2012, MNRAS, 421, 2264
- Kennedy G. M., et al., 2019, Nature Astronomy
- Kley W., Haghighipour N., 2015, A&A, 581, A20
- Kostov V. B., et al., 2016, ApJ, 827, 86
- Kostov V. B., et al., 2021, AJ, 162, 234
- Larwood J. D., Papaloizou J. C. B., 1997, MNRAS, 285, 288
- Larwood J. D., Nelson R. P., Papaloizou J. C. B., Terquem C., 1996, MNRAS, 282, 597
- Lodato G., Facchini S., 2013, MNRAS, 433, 2157
- Lodato G., Price D. J., 2010, MNRAS, 405, 1212
- Lodato G., Pringle J. E., 2007, MNRAS, 381, 1287
- Lubow S. H., Martin R. G., 2016, ApJ, 817, 30
- Lubow S. H., Martin R. G., 2018, MNRAS, 473, 3733

- Lubow S. H., Ogilvie G. I., 2000, *ApJ*, 538, 326
- Martin D. V., 2017, *MNRAS*, 465, 3235
- Martin R. G., Lubow S. H., 2017, *ApJ*, 835, L28
- Martin R. G., Lubow S. H., 2018, *MNRAS*, 479, 1297
- Martin R. G., Lubow S. H., 2019, *MNRAS*, 490, 1332
- Martin D. V., Triaud A. H. M. J., 2014, *A&A*, 570, A91
- Martin D. V., Triaud A. H. M. J., 2015, *MNRAS*, 449, 781
- Martin R. G., Nixon C., Armitage P. J., Lubow S. H., Price D. J., 2014, *ApJ*, 790, L34
- Martin R. G., Lubow S. H., Nixon C., Armitage P. J., 2016, *MNRAS*, 458, 4345
- Mayer L., Wadsley J., Quinn T., Stadel J., 2005, *MNRAS*, 363, 641
- McKee C. F., Ostriker E. C., 2007, *ARA&A*, 45, 565
- Monin J.-L., Clarke C. J., Prato L., McCabe C., 2007, *Protostars and Planets V*, pp 395–409
- Mösta P., Taam R. E., Duffell P. C., 2019, *ApJ*, 875, L21
- Muñoz D. J., Miranda R., Lai D., 2019, *ApJ*, 871, 84
- Murat Esmer E., Baştürk Ö., Osman Selam S., Aliş S., 2022, *arXiv e-prints*, p. arXiv:2202.02118

Nelson A. F., 2000, ApJ, 537, L65

Nixon C. J., 2012, MNRAS, 423, 2597

Nixon C. J., King A. R., Pringle J. E., 2011, MNRAS, 417, L66

Nixon C., King A., Price D., 2013, MNRAS, 434, 1946

Orosz J. A., et al., 2012, ApJ, 758, 87

Papaloizou J. C. B., Pringle J. E., 1983, MNRAS, 202, 1181

Papaloizou J. C. B., Terquem C., 1995, MNRAS, 274, 987

Picogna G., Marzari F., 2015, A&A, 583, A133

Pierens A., Nelson R. P., 2018, MNRAS, 477, 2547

Price D. J., 2007, PASA, 24, 159

Price D. J., Federrath C., 2010, MNRAS, 406, 1659

Price D. J., et al., 2018, PASA, 35, e031

Rein H., Tamayo D., 2015, MNRAS, 452, 376

Schneider J., 1994, Planet. Space Sci., 42, 539

Shakura N. I., Sunyaev R. A., 1973a, A&A, 24, 337

Shakura N. I., Sunyaev R. A., 1973b, A&A, 500, 33

Smallwood J. L., Franchini A., Chen C., Becerril E., Lubow S. H., Yang C.-C., Martin

R. G., 2020, MNRAS, 494, 487

Verrier P. E., Evans N. W., 2009, MNRAS, 394, 1721

Welsh W. F., et al., 2012, Nature, 481, 475

Winn J. N., Holman M. J., Johnson J. A., Stanek K. Z., Garnavich P. M., 2004, ApJ, 603, L45

Zanazzi J. J., Lai D., 2018, MNRAS, 473, 603

Zhang Z., Fabrycky D. C., 2019, ApJ, 879, 92

## CURRICULUM VITAE

Graduate College  
University of Nevada, Las Vegas

Charles Abod  
charlieabod@gmail.com

University of Nevada, Las Vegas  
4504 S. Maryland Parkway  
Las Vegas, Nevada 89154

### Degrees:

Bachelor of Arts, Physics, 2019  
University of Colorado, Boulder

Bachelor of Arts, Astrophysics & Planetary Sciences, 2019  
University of Colorado, Boulder

### Publications:

**Charles Abod**, Jacob Simon, Rixin Li, Philip Armitage, Andrew Youdin, Katherine Kretke. "The Mass and Size Distribution of Planetesimals Formed by the Streaming Instability. II. The Effect of the Radial Gas Pressure Gradient", ApJ, 883, 192

**Charles Abod**, Cheng Chen, Jeremy Smallwood, Ian Rabago, Rebecca Martin, Stephen Lubow. "Polar Alignment of a Massive Retrograde Circumbinary Disc Around an Eccentric Binary", MNRAS, (Submitted)

Thesis Title: Polar Alignment of Massive Retrograde Circumbinary Discs

### Thesis Examination Committee:

Chairperson, Dr. Rebecca G. Martin, Ph.D.  
Committee Member, Dr. Zhaohuan Zhu, Ph.D.  
Committee Member, Dr. Stephen Lepp, Ph.D.  
Graduate Faculty Representative, Dr. Laurel Raftery, Ph.D.